








# Distributed Multiuser MIMO for LiFi: Experiments in an Operating Room

Sreelal Maravanchery Mana , Volker Jungnickel , *Member, IEEE*, Kai Lennert Bober , Peter Hellwig, Jonas Hilt, Dominic Schulz , Anagnostis Paraskevopoulos, Ronald Freund, *Member, IEEE*, Klara Hirmanova, Radek Janca , Petr Chvojka , and Stanislav Zvanovec , *Senior Member, IEEE*

**Abstract**—Networked optical wireless communication, also denoted as LiFi, is expected to play an important role in so-called smart hospitals. In this paper, we present the first experimental study of LiFi in an operating room at Motol University Hospital in Prague, Czech Republic. First, we perform one-to-one measurements using an optical transmitter (Tx) and receiver (Rx) and observe that channels with a free LOS provide sufficient signal strength for mobile communication inside the operating room. Then we combine the individual LOS links into a multiple-input multiple-output (MIMO) link using four distributed transmitters representing a wireless infrastructure, and six distributed receivers representing medical devices. In this configuration, at least two strong singular values of the MIMO channel matrix are observed which allow spatial multiplexing. By appropriately clustering the transmitters and selecting the users, mobile devices can be served in parallel. For data transmission, several multiplexing schemes such as time-division multiple access (TDMA) with one and two best links, TDMA with spatial reuse, space-division multiple access (SDMA) with two best links with and without zero forcing (ZF) are considered. Results show that SDMA with ZF increases the data rate by 2.7 times compared to baseline TDMA, resulting in a total data rate of 600 Mbit/s.

**Index Terms**—Channel characterization, LiFi, MIMO, multiplexing, optical modulation, optical wireless communication, spatial diversity.

Manuscript received March 6, 2021; revised May 14, 2021 and June 9, 2021; accepted June 14, 2021. Date of publication June 22, 2021; date of current version September 18, 2021. This work was supported in part by the VisIoN Project, a European Union's H-2020 MSCA ITN program under Grant 764461. (Corresponding author: Sreelal Maravanchery Mana.)

Sreelal Maravanchery Mana, Volker Jungnickel, Kai Lennert Bober, Peter Hellwig, Jonas Hilt, Dominic Schulz, Anagnostis Paraskevopoulos, and Ronald Freund are with the Photonics Networks and Systems Department, Fraunhofer Heinrich Hertz Institute, 10587 Berlin, Germany (e-mail: sreelal.maravanchery@hhi.fraunhofer.de; volker.jungnickel@hhi.fraunhofer.de; kai.lennert.bober@hhi.fraunhofer.de; peter.hellwig@hhi.fraunhofer.de; jonas.hilt@hhi.fraunhofer.de; dominic.schulz@hhi.fraunhofer.de; anagnostis.paraskevopoulos@hhi.fraunhofer.de; ronald.freund@hhi.fraunhofer.de).

Klara Hirmanova is with the Department of Medical Technology, Motol University Hospital, 15006 Prague, Czech Republic (e-mail: klara.hirmanova@fnmotol.cz).

Radek Janca, Petr Chvojka, and Stanislav Zvanovec are with the Faculty of Electrical Engineering, Czech Technical University in Prague, 16627 Prague, Czech Republic (e-mail: jancarad@fel.cvut.cz; chvojka.petr@gmail.com; xzvanove@fel.cvut.cz).

Color versions of one or more figures in this article are available at <https://doi.org/10.1109/JLT.2021.3091385>.

Digital Object Identifier 10.1109/JLT.2021.3091385

## I. INTRODUCTION

THE increasing availability of robust and efficient optical wireless communication technologies will complement traditional medical services by supporting health-care through device automation besides efficient use of management and data. The present paper studies networked optical wireless communication (also denoted as Light Fidelity, LiFi [1] [2]) as an attractive solution for several health-care applications and to support the grand vision of the connected or smart hospital [3]–[5].

In the smart hospital, efficient communication will be an essential asset to ensure high quality treatment. All key stakeholders including patients, health-care personnel, equipment, data centers, and large number of Internet of things (IoT) nodes connect to the wireless infrastructure. The rapidly increasing number of medical sensors and devices, together with the intuitive trend towards using visual information, challenge the existing wireless technologies to go beyond their current limits in terms of spectrum reuse, data rates, reliability, security, and latency. Existing radio networks tend to reuse the spectrum increasingly. Wireless LANs currently realize and target area capacities of 1 and 10 Mbit/s/m<sup>2</sup>, respectively. However, as the number of devices continues to increase, cells will become even smaller. Thus, radio is limited. Interference from adjacent rooms, which can be quite complicated due to rich multi-path propagation, makes it hard to reach high area capacity.

LiFi does not penetrate through walls; LiFi cells in adjacent rooms can be isolated from each other. Moreover, propagation inside a room is mostly via line-of-sight (LOS). Thus, LiFi simplifies interference handling in very small cells. In hospitals, there are additional requirements to prevent electromagnetic interference (EMI) from medical devices [6]. Accordingly, the key advantages of LiFi are the use of license-free optical spectrum, provision of high data rates in small cells, inherently improved security inside the light beam, EMI-free wireless signaling, and very reliable data transmission [7]. For these reasons, LiFi appears as an alternative wireless communication technology, besides 5G and wireless LANs [8].

Recently, several research activities explored the potential of LiFi as wireless technology in the health-care sector [9]–[17]. LiFi based technologies can be used in hospital applications including a patient monitoring device [9], LiFi-enhanced robots



Fig. 1. Neurosurgical operating room of the Motol University Hospital in Prague, where the LiFi channel measurement took place.

for hospital transportation [10], medical wireless body area networks [11] [12], etc. The use case for LiFi considered in this paper is high-resolution real-time video streaming from cable-free medical devices such as video endoscopes, intubation aids, ultrasonic devices, hand-held X-ray or THz scanners etc., which provide immediate feedback to the surgeon while operating the patient. The increasing demand for 3D in surgery will further increase the data rate and latency requirements. It is common to use multiple devices on the same operating table providing different information to the surgeon. Per device, sustainable data rates of at least 100 Mbit/s are needed for compressed 4K video transfer at 24 frames per second. End-to-end latency should be below 80 ms, which include that images must be captured, processed, transmitted and displayed in real time.

Detailed channel characterization provides valuable support for the deployment of LiFi [12], since diffuse reflections might influence LiFi systems in any indoor scenario [11]. While there have been numerous studies of LiFi channels in indoor environments, see e.g., [13], surgery rooms differ significantly from conference rooms or offices. There are few windows through which light could escape, and most surfaces are white including objects and walls. The surgery room is illuminated brightly even with normal luminaires. Moreover, there are many objects in the surgery room, which increase the likelihood of blocking the LOS. Reliability against shadowing and blocking is another major challenge for LiFi systems. A single access point (AP) cannot always allow reliable connectivity. In earlier studies, we have shown that a promising idea is the use of multiple APs, ideally by using multiple-input multiple-output (MIMO) techniques [18], to provide highly reliable connectivity for mobile users in indoor scenarios [19],[20].

The first objective of this paper is to investigate the channel properties of LiFi in medical scenarios. Secondly, we show how to better utilize the potential of MIMO through spatial multiplexing, in addition to diversity. We conducted experiments in the children neurosurgical operating room, shown in Fig. 1, of the Motol University Hospital in Prague, Czech Republic in order to measure numerous LiFi channel responses. To our knowledge, we were the first to conduct such measurements. Measurement

data are used for performance analysis considering the plurality of links between all transmitters and all receivers as a distributed multiuser (MU) MIMO link. Therefore, we consider different transmission schemes to enable robust communication over the LiFi system and compare the achievable data rates.

Our results demonstrate the possibility to provide individual data rates of at least 30 Mbit/s for each device and a sum data rate higher than 500 Mbit/s for all devices on the operating table. Preliminary results were published in [21]. In this paper, we extend our study and provide the following main contributions:

- Systematic experimental channel characterization of a LiFi system within a surgery room
- Complete mathematical framework for several multiplexing algorithms with different complexity considering LiFi as a distributed MU-MIMO link
- Quantification of the performance limits when using these algorithms based on measurements and simulations in a real medical scenario

The remainder of the paper is organized as follows. Section II describes the LiFi channel measurement campaign and discusses the experimental setup and all transmitter (Tx) receiver (Rx) configurations. Section III reports the measurement results and basic channel parameters. The analysis of the individual links leads to consider the scenario as a distributed MU-MIMO link, which is introduced in Section IV. Section V introduces different multiuser multiplexing schemes and provides a theoretical framework for obtaining the effective signal to interference plus noise ratio (SINR) and estimation of the throughput. Finally, the performance is analyzed and conclusions are given in Sections VI and VII, respectively.

## II. LiFi CHANNEL MEASUREMENT CAMPAIGN

The deployment of LiFi in medical scenarios is considered more challenging than in regular office rooms due to the presence of multipath signals associated with diffuse reflections from white-painted walls, ceiling, floor as well as furniture, and a high number of medical devices. Moreover, the latter lead to more frequent obstructions of the LOS paths than in office rooms. A thorough channel characterization, which gives a better understanding of the corresponding optical wireless communication channel, is an essential prerequisite for the design of a reliable, high-performance medical LiFi system.

In our particular medical scenario, the communication for the existing systems is located around the operating table. Our main idea is to replace the existing cable-based communication links by new optical wireless links. We exploit short links with a free LOS to multiple optical wireless access points mounted at the ceiling. The measurements are conducted in the downlink. Assuming that optical frontends are reciprocal (i.e., have the same beam characteristics in up- and downlink), the measurement data can also be used to characterize the uplink channel.

In this section, we provide detailed information about our experimental setup in the operating room, the measurement method, and the considered Tx and Rx configurations for the channel characterization.

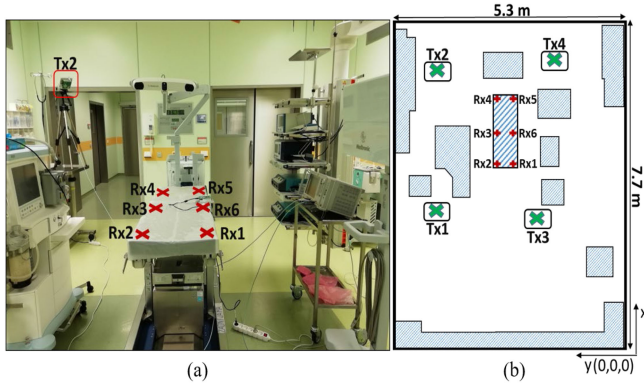


Fig. 2. LOS LiFi-configurations. (a) The measurement scenario, Rx positions are marked in red. (b) Top view of the room, Tx and Rx positions are marked in green and red color, respectively. Shaded area show further LOS obstacles in the room.

### A. Experimental Setup

A vector network analyzer (VNA, Agilent E5061B-3L5), connected between optical Tx and Rx, is used to measure the frequency responses for all Tx-Rx configurations of the communication system. Our optical frontend consists of four infrared (IR) light-emitting diodes (LEDs) (SFH 4715AS) at 850 nm connected in parallel and fed from the same driver circuit to send high optical power into the coverage area. At the Rx, five photodiodes (PDs) (Hamamatsu S6968) are used to increase the overall detection area and collect more optical power. Each PD has its own bootstrap amplifier, after which equal gain combining is applied in the electrical domain. The LED has 45° half-angle for the radiation beam and the PD has 30° half-angle for the field of view (FOV). This ensures a wide coverage area and enables mobile optical communication. In this setup, the optical power is boosted by a factor of 20 by using four LEDs and five PDs, yielding a gain of 26 dB in the electrical domain compared to a frontend using a single LED and PD each. This gain significantly improves the detectability of the weak optical wireless signals in realistic mobile scenarios [22] and in some settings even supports non-line-of-sight (NLOS) wireless communications. The used optical frontends are optimized for a smooth roll-off towards higher frequencies, with cut-off frequencies of -3 dB frequency at 80 MHz, and -10 dB at 135 MHz, see Fig. 2 in [22].

### B. Channel Response Calibration

Measurements are carried out using the classical continuous wave (CW) frequency-sweep technique [23]. The VNA provides a CW signal with 0 dBm electrical power to the optical Tx, where the modulation frequency of the LED varies from 1 MHz to 200 MHz. Due to the bandwidth limitation in our frontend, we keep the maximum sweeping frequency at 200 MHz. The VNA compares the amplitude and phase of the transmitted signal with the received signal, and thereby delivers the complex-valued frequency response of the device-under-test (DUT). In our case, the DUT comprises the wireless link and the optical frontends.

TABLE I  
POSITIONS OF OPTICAL FRONTENDS IN LOS CONFIGURATIONS

Optical frontends (OFE)	Positions in m (x, y, z)
Tx1	(3.25, 4.3, 2.1)
Tx2	(6.7, 4.3, 2.1)
Tx3	(3, 1.85, 2.2)
Tx4	(6.95, 1.5, 2.2)
Rx1	(4.4, 2.6, 1)
Rx2	(4.4, 2.9, 1)
Rx3	(5, 2.9, 1)
Rx4	(6, 2.9, 1)
Rx5	(6, 2.6, 1)
Rx6	(5, 2.6, 1)

The measured overall frequency response of the LiFi system is represented as

$$H_{Sys}(f) = H_{Rx}(f) \cdot H_{Ch}(f) \cdot H_{Tx}(f), \quad (1)$$

where  $H_{Rx}(f)$  is the frequency response of the Rx,  $H_{Tx}(f)$  is the frequency response of the Tx and  $H_{Ch}(f)$  represents the frequency response of the LiFi channel.

For characterizing the LiFi propagation channel, the impact of the frontends has to be removed [22]. For this reason, a calibration is performed by keeping the Tx and Rx in the reference LOS distance  $d_{ref}$  of 1 m. The reference distance  $d_{ref}$  is selected so that the link has negligible distortion, i.e., no signal clipping or saturation is observed at the receiver. The reference channel response is given as

$$H_{Ref}(f) = H_{Rx}(f) \cdot H_{d_{ref}}(f) \cdot H_{Tx}(f), \quad (2)$$

where  $H_{d_{ref}}(f)$  is the frequency response of the LOS reference channel. Correspondingly, a normalized frequency response of the LiFi channel is obtained as

$$H_{Ch_{norm}}(f) = \frac{H_{Sys}(f)}{H_{Ref}(f)} = \frac{H_{Ch}(f)}{H_{d_{ref}}(f)}. \quad (3)$$

Based on  $H_{Ch_{norm}}(f)$ , all other channel parameters such as channel impulse response (CIR), root-mean-square (RMS) delay spread, as well as path loss can be determined [22]. In the remainder of this paper, we consider the channel response as the obtained data from equation (3), i.e., the impact of the optical frontends is always removed. Accordingly, the LOS reference channel response  $H_{d_{ref}}(f)$  is represented by 0 dB in the amplitude response of the normalized LiFi channels [22].

### C. Tx-Rx Configurations

The considered LOS measurement scenario is shown in Fig. 2(a). In this case, we investigate the performance of the LiFi system deployed in an operating room (with dimensions of 5.3 m x 7.7 m x 3 m). The Tx is placed at four different positions, Tx1, Tx2, Tx3, and Tx4, close to the ceiling in the neurosurgical operating room. The Rx is placed at six positions on the operating table labelled as Rx1 to Rx6 as shown in Fig. 2(b). The exact positions of all optical frontends inside the room are given in Table I. The Tx positions, Tx1 and Tx3 are closer to the patient's

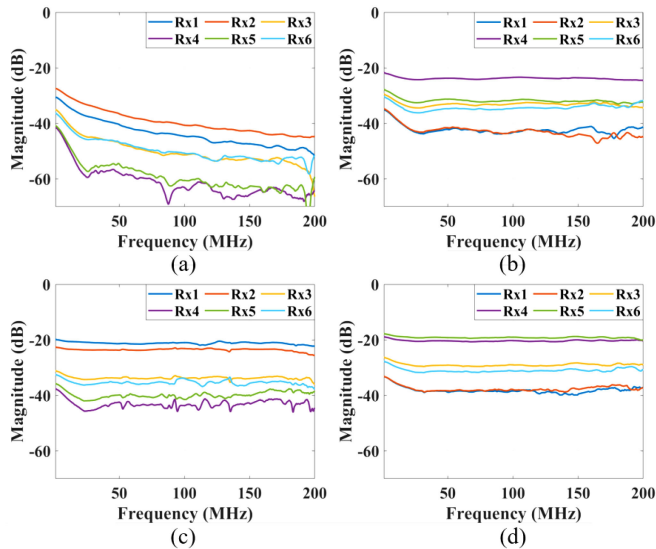


Fig. 3. Amplitude responses of LiFi channels in LOS configurations for different combinations of Tx and Rx: (a) Tx1, (b) Tx2, (c) Tx3, and (d) Tx4.

head, whereas Tx2 and Tx4 are closer to the patient’s legs. Rx1 and Rx2 are placed at the head position of a patient, Rx3 and Rx6 are located at the center position of the operating table and Rx4 and Rx5 are at the leg position. In general, in the considered scenario, the transmitters point towards the operating table and the receivers point towards the ceiling.

### III. CHANNEL MEASUREMENT RESULTS

In this section, channel measurement results are reported and discussed for the various Tx-Rx configurations described in the previous section. The intention is to provide fundamental insights into point-to-point channel characteristics before investigating complex networked LiFi channels with multiple transmitters and multiple users.

#### A. Channel Response

The measured amplitude responses of the LOS channels corresponding to all positions of Tx and Rx (given in Table I) are shown in Fig. 3. Here, Rx1 and Rx2, placed around the patient’s head, experience free LOS links from Tx1 and Tx3. Similarly, Rx4 and Rx5, placed nearby the patient’s legs, have free LOS links from Tx2 and Tx4. The amplitude responses of the strong LOS signals are almost flat. If the LOS is weaker, non-LOS signals have more chance to interfere destructively [22]. The amplitude responses for Rx3 and Rx6 always lie between the best and worst case responses since both receivers are located at a central position of the operating table. The initial drop (around 3 to 18 dB, depending on the transmitter configurations) at low frequencies indicates that there are many diffuse reflections in the surgical room due to a number of objects with diffusely reflecting bright colors. A similar phenomenon is explained in [24]. Flatness at higher frequencies in the amplitude response indicates the presence of a strong LOS signal in the channel.

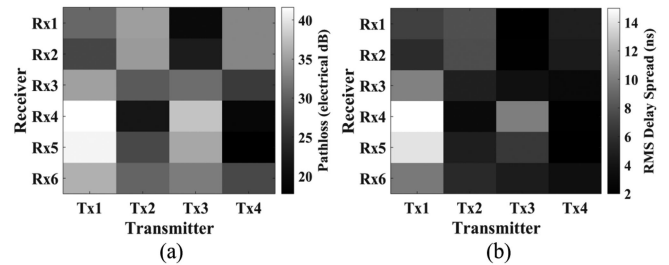


Fig. 4. Channel parameters for LOS scenarios: (a) path loss of the channel and (b) RMS delay spread of the channel.

In addition, higher-order reflections occur in the operating room. These, however, have a significantly higher path loss due to diffuse scattering and multipath propagation over longer distances. It is well known that in case of such NLOS links, the received signal strength depends on the area of overlap between the area covered by the FOV of the PDs and the area irradiated by the LEDs [22]. The measurement results of NLOS channels are explained in more detail in the Appendix. They suggest that NLOS communication is possible in the medical scenario but with lower bandwidth and SNR. Correspondingly reduced data rates are acceptable, e.g., for low-rate services like wireless control applications. As we aim for high throughput in this paper, we focus on configurations with free LOS from now on.

#### B. Channel Parameters

Further systematic characterization of the LiFi channel is possible by estimating the main channel parameters such as path loss and RMS delay spread. We have calculated the path loss at the lowest modulation frequency of 1 MHz and the RMS delay spread from the frequency-domain measurement as described in [22]. The parameters are shown in Fig. 4(a) and Fig. 4(b), respectively. The path loss is mainly due to the geometrical loss between the optical frontends, Tx and Rx. From our experimental data, we attribute the RMS delay spread values below 9 ns to strong LOS and values above 9 ns to weak LOS. Obviously, 9 ns represents the effective time resolution of our measurement system.

The above channel responses and parameters depend heavily upon the position of optical frontends, possible link blockage, and diffuse reflections. However, high-speed data links require sufficient signal strength and wide bandwidth. Therefore, LOS channels are favorable for intended high-speed communication scenarios.

Previous studies show that the combination of multiple links exploits *spatial diversity* and yields one robust communication link [18], [19]. But, in many cases, multiple links can also be used for *spatial multiplexing*, i.e., transmitting data over multiple links in parallel towards multiple mobile devices to increase system throughput. Since the operating room scenario consists of multiple access points and multiple mobile devices, the question arises how the LiFi system can be designed so that a reliable high-speed communication between these units is enabled.

#### IV. DISTRIBUTED MU-MIMO CONCEPT

In general, wireless systems optimize the single link, either by providing separate time slots for separate users like in Wi-Fi systems or by coordinating the potential interference, like in traditional cellular networks. In the Long Term Evolution (LTE) advanced system, there are new transmission techniques denoted as distributed MIMO or joint transmission coordinated multi-point (JT-CoMP) [25], [26]. These techniques consider the many links between all base stations and all mobile users as one huge distributed MIMO, which is coordinated by a central controller. Note that, this approach enables both higher data rates and lower latency [27]. Here, we follow this approach in order to optimize the performance.

In this section, we consider the links between many optical access points to many mobile devices as a distributed multiuser MIMO link, which can be formed by using the measured LOS channel responses for the individual Tx and Rx links. Our aim is to show that, based on the measured channels presented in the previous section, reliable data transmission can be realized more efficiently than in the existing LiFi systems. Therefore, we consider the optical access points and mobile devices as inputs and outputs of a MIMO link, based on the experimental results of LOS configuration (Fig. 2). Next, we discuss the structure of singular values of the corresponding MIMO channel matrix. In this MIMO architecture, we assume that all transmitters are coordinated from a central unit, which enables simultaneous transmissions from multiple transmitters, i.e., spatial diversity, to prevent sudden blockages of the LOS links. Moreover, coordinated parallel transmissions to multiple mobile devices are possible by using the space and time domains [28], [29], [30].

The MU-MIMO link is characterized by using the singular values. The MIMO channel matrix, for the considered LOS scenario described in Fig 2, at a given  $i^{th}$  frequency  $f_i$  is

$$H(f_i) = \begin{bmatrix} H_{11}(f_i) & \cdots & H_{14}(f_i) \\ \vdots & \ddots & \vdots \\ H_{61}(f_i) & \cdots & H_{64}(f_i) \end{bmatrix}, \quad (4)$$

which includes frequency responses of the channels between all the transmitters and receivers. Singular value decomposition (SVD) of the MIMO channel matrix  $H = U \cdot D \cdot V^H$  is a mathematical tool, which removes the cross-talk among the individual signals in the MIMO channel after the multiplication of the received and transmitted signal vectors with the unitary matrices  $U^H$  and  $V$ , respectively [31]. The matrix  $D$  is called a quasi-diagonal matrix with positive real-valued entries and it has the same matrix dimension as  $H$ . Multiple non-zero singular values show that parallel data transmission is possible over the wireless channel [32]. The SVD proves that the maximum number of data streams that can be transmitted in parallel is given by the minimum of  $(n_{Tx}, n_{Rx})$  if the channel matrix has full rank, where  $n_{Tx}$  is the number of transmitters and  $n_{Rx}$  is the number of receivers [33]. However, the useful number of data streams depends on the considered wireless scenario.

In our configuration, we calculated the singular values at each frequency point as shown in Fig. 5(a). The first two singular values,  $\lambda_1$  and  $\lambda_2$ , are significantly higher than the other singular

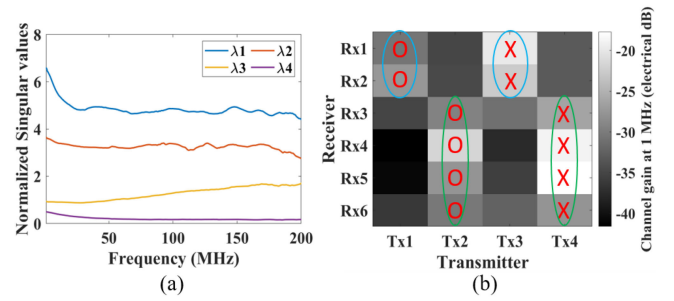


Fig. 5. Distributed MU-MIMO based on LOS scenario (see Fig. 2) (a) singular values,  $\lambda_1$ ,  $\lambda_2$ ,  $\lambda_3$  and  $\lambda_4$ , of the 4x6 MIMO channel. (b) channel gain at 1 MHz. Here, first maxima indicated as X and second maxima as O. First data stream, encircled in blue color, is sent by Tx1 and Tx3. Second data stream, encircled in green color, is sent by Tx2 and Tx4.

values  $\lambda_3$  and  $\lambda_4$ . Accordingly, at least two data streams can be spatially multiplexed, i.e., transmitted in parallel, in our particular MU-MIMO scenario. In order to understand how to coordinate the data transmission between each Tx and Rx, we calculated the channel gain (see Fig. 5(b)), which is equal to the negative of path loss at the lowest modulation frequency shown in Fig. 4(a). The channel gain shows that each Rx has at least two strong Tx links. In our scenario, using more transmitters would increase complexity, put additional burden on the backbone and limit the opportunities for parallel transmission to multiple users in the room. From our observations, it is intuitive that Tx1 and/or Tx3 can send the first data stream to Rx1 or Rx2. In addition, Tx2 and/or Tx4 can send the second data stream to Rx3, Rx4, Rx5 or Rx6. In this way, each Rx may obtain its data signals from the intended transmitters and potential interference from other transmitters. The availability of two links for each user ensures a reliable transmission even if one LOS path is blocked, while the other link is free.

However, coordination is needed to support the simultaneous data transmission to multiple users. In the following, we consider five possible multiplexing schemes. As a baseline, we consider time division multiple access (TDMA) by using only the best link. The other schemes are TDMA with two best links, TDMA with uncoordinated spatial reuse, space division multiple access (SDMA) with two best links, and SDMA with zero forcing (ZF). For each multiplexing scheme, a mathematical framework is required to define the clustering of the transmitters and the selection of receivers for an effective communication. In the next section, we discuss this framework in detail based on the defined distributed MIMO concept given above.

#### V. FRAMEWORK FOR DISTRIBUTED MU-MIMO

The motivation for implementing different multiplexing schemes is to compare the performance and show how efficient communication is possible in a distributed MU-MIMO architecture. In all schemes, a suitable allocation of time and space resources is required. This section describes a detailed mathematical framework of the considered multiplexing schemes and the corresponding throughput estimation method for the LiFi-system.

In the MU-MIMO system, the output signal is expressed as

$$y = G \cdot d + noise, \quad (5)$$

where  $G$  is the effective channel matrix and  $d$  is the vector which contains all input data streams. The effective channel matrix is given as

$$vvG = R_m^T \cdot (H \cdot T_n), \quad (6)$$

where  $m = 1, 2, \dots, n_{Rx}$  and  $n = 1, 2, \dots, n_d$ . While the total number of transmitters is four and the total number of receivers is six, we limit the total number of data streams  $n_d = 2$ , as justified in the previous section.

The matrix  $T_n$  is a  $(n_{Tx} \times n_d)$  matrix,  $R_m$  is a  $(n_{Rx} \times n_d)$  matrix,  $H$  is a  $(n_{Rx} \times n_{Tx})$  MIMO channel matrix, and the effective channel matrix  $G$  is a  $(n_d \times n_d)$  matrix. The diagonal elements in  $G$  represent the signal intended for the receivers and non-diagonal elements represent the interference. The matrices  $T_n$  and  $R_m$  are used to select the Tx and Rx during each transmission in the given time slot. Each element in the matrix  $T_n$ ,  $t_{l,n}$ , is equal to one if  $l^{\text{th}}$  Tx is active during the transmission of  $n^{\text{th}}$  data stream and is equal to zero otherwise, where  $l = 1, 2, \dots, n_{Tx}$ . Each element in the matrix  $R_m$ ,  $r_{m,n}$ , is equal to one if  $m^{\text{th}}$  Rx is receiving when  $n^{\text{th}}$  data stream is transmitted and is equal to zero otherwise.

Based on these selection matrices, various multiplexing schemes can be described. Correspondingly, we numerically analyze the SINR and throughput for the considered multiplexing schemes. We assume that all transmitters have the same power in the given time, i.e.,  $P_{Txl} = P_{Tx}$ .

#### A. TDMA With One Best Link

In the case of TDMA, each user is assigned a particular time slot with the full channel bandwidth for the link [28], a method also supported by the ITU-T standard G.9991, which is widely used for LiFi systems [34]. In our case, we consider six time slots in total available to communicate with all receivers, where each receiver receives the data stream one after the other. In each link, the transmitter, which has the best signal strength, sends the data stream. Therefore, during the first two time slots, Tx3 sends the first data stream  $d_1$  and the remaining four time slots Tx4 sends the second data stream  $d_2$  to corresponding receivers.

At first, the 2x2 effective channel matrix  $G$  corresponding to each time slot is calculated using the equation (6). For example,  $G$  corresponding to Rx1 during the first time slot is

$$G_{Rx1} = \begin{bmatrix} H_{13} & 0 \\ 0 & 0 \end{bmatrix}. \quad (7)$$

From equation (5), the signal received at Rx1 is calculated as

$$y_{Rx1} = G_{Rx1} \cdot d_1 + noise. \quad (8)$$

After substituting the effective channel matrix, the received signal power at the Rx1,  $P_{Rx1}$ , is defined as

$$P_{Rx1} = P_{Tx} \cdot |H_{13}|^2. \quad (9)$$

Since there is no off-diagonal term in the effective channel matrix, no interference is received. In a similar way, we calculated the received signal power at every Rx corresponding to each time slot.

The SINR is the ratio between the received signal power to the sum of interference power and noise power. In this paper, we consider the noise power as the noise that can be generated at the reference distance (i.e., calibration distance  $d_{ref}$ ). In the reference case, with respect to the signal to noise ratio (SNR) at the receiver side, the received noise power can be expressed as

$$P_N = \frac{|H_{Ref}|^2 \cdot P_{Tx}}{SNR_{ref}}. \quad (10)$$

The SINR at the Rx1 during the first time slot is given as

$$SINR_{Rx1} = \frac{P_{Rx1}}{P_N} = \frac{|H_{13}|^2}{SNR_{ref}}. \quad (11)$$

We assume that the maximum achievable  $SNR_{ref}$  of our LiFi modules is 45 dB at the reference distance. In our previous channel measurements [35], using the same optical frontends, we observed that signals having channel gain below 45 dB are not detectable. Thus, 45 dB is the maximum achievable SNR when using a constant envelope signal. For the throughput estimation, however, the modulation scheme and non-linear effects have to be considered. When connecting the same frontends at the same distance to a direct current (DC) biased orthogonal frequency-division multiplexing (OFDM) chipset based on G.9991 with 200 MHz bandwidth, maximum SNR of 35 dB has been measured with 1 Gbit/s data rate. The reduction in SNR is due to the reduced modulation current in order to avoid clipping. Next, we explain how to estimate the achievable throughput based on channel measurements.

Therefore, according to equation (10), we have considered the noise power as a constant value lying -45 dB below the maximum value of  $|H_{Ref}|^2 \cdot P_{Tx}$ . In other words, it is the minimum noise that could be generated at the LiFi modules. We believe that signals below this level are not detectable at the receivers.

Similarly, we calculated the SINR for all other receiver positions, specifically for each time slot. Using the modified Shannon equation [36] and by inserting the SINR from our measurements, we can calculate the throughput at each Rx as

$$T = \Delta B \cdot \log_2 \left( 1 + \frac{SINR}{\Gamma} \right), \quad (12)$$

where  $\Delta B = 200$  kHz is the bandwidth over each frequency bin,  $\Gamma = 10$  is an empirically determined ‘‘gap’’ taking into account limited modulation amplitude to avoid clipping (as explained above), imperfect constellation shaping, and limited code word length. Equation (12) is applied on each frequency bin from 1 MHz to 200 MHz. We assume that, the data transmission adopts the uniform power spectral density over optimized frontends with smooth roll-off until 200 MHz. For computing the throughput for a particular Rx, summation of (12) applies over the entire bandwidth.

The throughput corresponding to each Rx is further multiplied with the allotted time, i.e., 1/6 of the total time. Finally, the

summation of the throughputs of all receivers results in the total throughput of the TDMA with one best link scheme.

### B. TDMA With Two Best Links

In this scheme, for each receiver, we have combined the two best transmitters for communication. The first two time slots are available for the communication of Tx1 and Tx3, first with Rx1 and then with Rx2. Another four time slots are assigned for the data transmitted by Tx2 and Tx4 to the other receivers, one after another.

At first, the effective channel matrix  $G$  for each time slot is calculated using equation (6). For example, the effective channel matrix corresponding to the signal received at Rx1 during the first time slot is given as

$$G_{Rx1} = \begin{bmatrix} H_{11} + H_{13} & 0 \\ 0 & 0 \end{bmatrix}. \quad (13)$$

We consider that the first data stream  $d_1$  is transmitted jointly by Tx1 and Tx3 to Rx1. Here, the signal received at Rx1 is calculated as same as given in (8). After substituting the effective channel matrix, the received signal power at the Rx1  $P_{Rx1}$  is given as

$$P_{Rx1} = P_{Tx} \cdot (|H_{11} + H_{13}|^2). \quad (14)$$

In a similar way, we have calculated the received signal power at every Rx in each time slot. By assuming the same noise power as given in (10), the SINR for each Rx is calculated. For example, the SINR at Rx1 during the first time slot is given as

$$SINR_{Rx1} = \frac{P_{Rx1}}{P_N} = \frac{(|H_{11} + H_{13}|^2)}{\frac{|H_{Ref}|^2}{SINR_{Ref}}}. \quad (15)$$

Likewise, SINR and then throughput for all other receivers are calculated as explained in section V. A.

### C. TDMA With Spatial Reuse

In this case, we consider two communication links with the least mutual interference in each time slot in order to realize the parallel data streams. This approach is widely used in Wi-Fi and cellular systems if the mutual interference is weak enough. As in the previous scenarios, at the first link, each receiver receives the data stream from the transmitter with the best signal strength. In parallel to this, on the second link, the transmitter that creates the least interference with respect to the first receiver sends the data to its own best receiver. For example, during the first time slot, Tx3 sends the first data stream to Rx1 and, in parallel, Tx2 sends the second data stream to Rx4. Similarly, we consider parallel communications in all time slots. Due to less interference, the link between Tx2 to Rx4 acts as a secondary link for the first two time slots and the link between Tx1 to Rx2 acts as a secondary link for the next four time slots.

All effective channel matrices have been computed for each time slot. For example, the effective channel matrix corresponding to the first time slot is given as

$$G_1 = \begin{bmatrix} H_{13} & H_{12} \\ H_{43} & H_{42} \end{bmatrix}. \quad (16)$$

Using equation (5), the received signal during the first time slot is given as

$$\begin{bmatrix} y_1 \\ y_2 \end{bmatrix} = G_1 \cdot \begin{bmatrix} d_1 \\ d_2 \end{bmatrix} + noise. \quad (17)$$

In the first time slot, first data stream  $d_1$  is transmitted from Tx3 and the signal power at Rx1 is defined same as equation (9).

Due to parallel communication, the data stream  $d_2$  send from Tx2 contributes to the interference at Rx1 and interference signal power at Rx1  $I_{Rx1}$  is given by

$$I_{Rx1} = P_{Tx} \cdot |H_{12}|^2. \quad (18)$$

Similarly, the received signal and interference power levels at Rx4 during the first time slot are given as

$$P_{Rx4} = P_{Tx} \cdot |H_{42}|^2, \quad (19)$$

$$I_{Rx4} = P_{Tx} \cdot |H_{43}|^2. \quad (20)$$

Likewise, the received signal and interference power levels at every Rx in the given time slot are calculated. By assuming the same noise power as given in (10), the SINR for each Rx is calculated for each time slot. For example, the SINR at Rx1 during the first time slot is given as

$$SINR_{Rx1} = \frac{P_{Rx1}}{I_{Rx1} + P_N} = \frac{(|H_{13}|^2)}{|H_{12}|^2 + \frac{|H_{Ref}|^2}{SINR_{Ref}}}. \quad (21)$$

Likewise, the SINR and then the throughput corresponding to all receivers are calculated as explained in section V. A.

### D. SDMA With Two Best Links

In this case, Rx1 and Rx2 share the total allocated time (i.e., half for each) to communicate with Tx1 and Tx3 and receive the signal one after the other. Spatially multiplexed with this transmission, at the same time, other receivers, Rx3 to Rx6, share the allocated time quarterly and receive the second data stream transmitted by Tx2 and Tx4. Accordingly, for the first stream, the first two time slots are for Rx1 and further two time slots are for Rx2. In parallel with this, for the second stream, each Rx is allocated with a single time slot. Thus, this multiplexing scheme has only four time slots in total.

The transmitter selection matrix consists of nonzero elements in all the columns and is given by

$$T = \sum_{n=1}^{n_d} T_n = \begin{bmatrix} 1 & 0 \\ 0 & 1 \\ 1 & 0 \\ 0 & 1 \end{bmatrix}. \quad (22)$$

The receiver selection matrix  $R_m$  is the same as in the previous scenario. The effective channel matrix given in (6) can be modified as

$$G = R_m^T \cdot (H \cdot T). \quad (23)$$

Using (23), the effective channel matrices corresponding to each Rx are calculated. For example, the effective channel matrix calculated at Rx1 during the first time slot is given as

$$G_{Rx1} = \begin{bmatrix} H_{11} + H_{13} & H_{12} + H_{14} \\ 0 & 0 \end{bmatrix}. \quad (24)$$

From (5), the signal received at Rx1 during the first time slot is represented as

$$y_{Rx1} = G_{Rx1} \cdot \begin{bmatrix} d_1 \\ d_2 \end{bmatrix} + noise. \quad (25)$$

The data stream  $d_1$  is the signal that Rx1 intends to receive. The signal power at the Rx1 is given as

$$P_{Rx1} = P_{Tx} \cdot (|H_{11} + H_{13}|^2). \quad (26)$$

The data stream  $d_2$  contributes to the interference at Rx1. The interference signal power at Rx1  $I_{Rx1}$  is given by

$$I_{Rx1} = P_{Tx} \cdot (|H_{12} + H_{14}|^2). \quad (27)$$

Similarly, the received signal and interference power levels at every Rx in the given time slot are calculated. As in previous scenarios, the SINR for each Rx is calculated. For example, the SINR at Rx1 during the first time slot is given as

$$SINR_{Rx1} = \frac{(|H_{11} + H_{13}|^2)}{(|H_{12} + H_{14}|^2) + \frac{|H_{Ref}|^2}{SNR_{Ref}}}. \quad (28)$$

Likewise, the SINR and throughput are calculated as explained in section V. A. However, here the throughput corresponding to each Rx is multiplied with a different time factor, i.e., 1/2 for Rx1 and Rx2 and 1/4 for the other receivers.

### E. SDMA With ZF

In the SDMA approach, there are interference terms in the non-diagonal elements of the effective channel matrix. To avoid interference in the multiuser scenario the zero forcing (ZF) algorithm is implemented in addition to the SDMA scheme with two best links in the following scheme.

Considering parallel communication, the transmitter selection matrix  $T$  is same as in equation (22). The receiver selection matrix  $R$  is the summation of all  $R_m$  matrices corresponding to the active receivers in the given particular time slot.

Accordingly, the effective channel matrix given in equation (6) is modified as

$$G = R^T \cdot (H \cdot T). \quad (29)$$

Depending on the channel, the ZF pre-coder generalizes the so-called channel inversion for multiple receivers in a given time slot. A Moore-Penrose pseudo-inverse of the effective channel gain matrix  $G$  is calculated as described in [37]. To avoid signal

clipping and ensure equal transmission power for all users, the pre-coder output is normalized so that all columns of the pre-coder matrix have the same norm [37]. Note that the inverse is computed for each time slot.

The output signal at  $j^{th}$  time slot is expressed as

$$y_j = G_j \cdot (G_j^{-1} \cdot K_j \cdot d) + noise, \quad (30)$$

where, the  $G_j$  is the 2x2 effective channel matrix at  $j^{th}$  time slot,  $G_j^{-1}$  is the Moore Penrose pseudo-inverse matrix of the effective channel matrix  $G_j$ ,  $d$  is data stream sent at each time slot and can be considered as a matrix  $\begin{bmatrix} d_1 \\ d_2 \end{bmatrix}$ . Finally,  $K$  is the normalization matrix during  $j^{th}$  time slot given as

$$K_j = \begin{bmatrix} 1/A_j & 0 \\ 0 & 1/B_j \end{bmatrix}. \quad (31)$$

The elements  $A_j$  and  $B_j$  are given as

$$A_j = \sqrt{|G_j^{-1}(1,1)|^2 + |G_j^{-1}(1,2)|^2} \quad (32)$$

$$B_j = \sqrt{|G_j^{-1}(2,1)|^2 + |G_j^{-1}(2,2)|^2}, \quad (33)$$

which are the two row norms for the inverse  $G_j^{-1}$  of the effective channel matrix. From equation (29), the effective channel matrix in the first time slot is given as

$$G_1 = \begin{bmatrix} H_{11} + H_{13} & H_{12} + H_{14} \\ H_{31} + H_{33} & H_{32} + H_{34} \end{bmatrix}. \quad (34)$$

Note that the data amplitudes are attenuated after passing through the pre-coder. This is visible in the final pre-coded channel matrix, which is given as

$$G_{prec} = (G_1 \cdot G_1^{-1} \cdot K) = \begin{bmatrix} 1/A_1 & 0 \\ 0 & 1/B_1 \end{bmatrix}. \quad (35)$$

Without considering the noise, the received signal during the first time slot is given as

$$\begin{bmatrix} y_1 \\ y_2 \end{bmatrix} = G_{prec} \cdot \begin{bmatrix} d_1 \\ d_2 \end{bmatrix}. \quad (36)$$

Here in the first time slot,  $d_1$  is sent by Tx1 and Tx3 to Rx1 and  $d_2$  is sent by Tx2 and Tx4 to Rx3. The SINR at Rx1 during the first time slot is given as

$$SINR_{Rx1} = \frac{(|G_{eff1}(1,1)|^2)}{\frac{|H_{Ref}|^2}{SNR_{Ref}}}. \quad (37)$$

Similarly, the SINR at Rx3 during the first time slot is

$$SINR_{Rx3} = \frac{(|G_{eff1}(2,2)|^2)}{\frac{|H_{Ref}|^2}{SNR_{Ref}}}. \quad (38)$$

Likewise, the SINR and throughput are calculated for every Rx as explained in section V. D. However, here the interference has been removed.



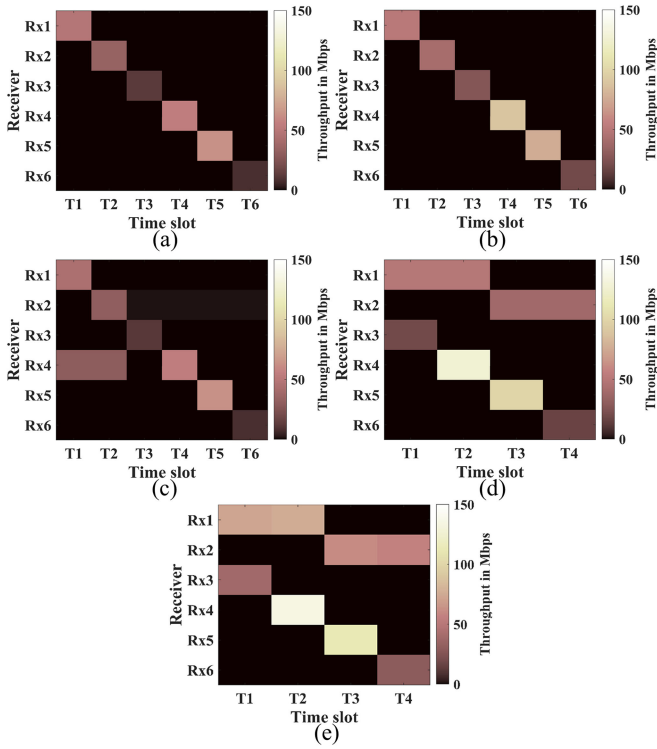


Fig. 6. Throughput at each Rx in each time slot: (a) TDMA with one best link, (b) TDMA with two best links, (c) TDMA with spatial reuse, (d) SDMA with two best links, and (e) SDMA with ZF.

## VI. DISTRIBUTED MU-MIMO RESULTS

Based on the measured 4x6 distributed MIMO channel responses, as well as the mathematical description of the multiplexing schemes in the previous section, the throughput has been calculated for the considered operating room scenario. The estimated user and total system throughputs of all investigated configurations are shown in Fig. 6 and Fig. 7.

In Fig. 6, the throughput in each time slot for each Rx is shown. The data rates depend on three factors: allotted time for each Rx, channel response, and possible interference from other transmitters. In our MIMO configuration, Rx4 and Rx5 have the best channel gains while Rx3 and Rx6 have the worst. The allotted time for each Rx is the same for all receivers in the first two cases, see Fig. 6(a) and (b). Even though the duration of each time slot is the same in TDMA with spatial reuse (Fig. 6(c)), via parallel communication, Rx4 and Rx2 are served in further time slots. In the other two multiplexing schemes, shown in Fig. 6(d) and (e), Rx1 and Rx2 have twice the allotted time compared to other receivers. By combining signals from the two best transmitters, the throughput for every Rx improves as compared to TDMA with one link scenario. Here, TDMA with spatial reuse and SDMA with two best links are the two schemes where interference affects the data transmission. The interference is higher for Rx3 and Rx6 when compared to other receivers. As shown in the previous section, the ZF method successfully nullifies the interference together with SDMA with two best links scheme and, accordingly, improves the performance for

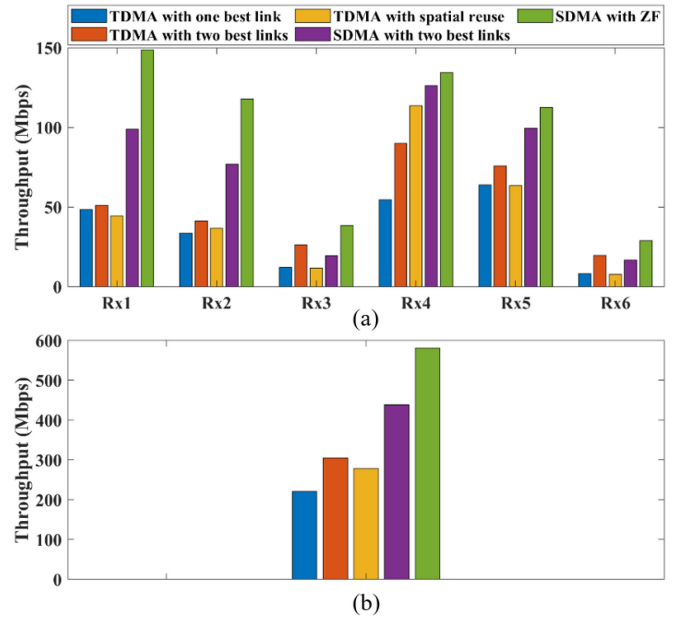


Fig. 7. Throughput results: (a) individual throughput for each Rx and (b) total throughput of the distributed MU-MIMO system.

all receivers. This leads to a significant improvement in the throughput of all receivers.

The individual throughput for each Rx corresponding to each multiplexing scheme is shown in Fig. 7(a). For Rx1, a data rate of around 48 Mbps is achieved using TDMA with one best link, which improves to around 51 Mbps by using the second best transmitter, too. TDMA with spatial reuse reduces the data rate of Rx1 to 46 Mbps due to the interference. SDMA with two best links increases the data rate for Rx1 to around 100 Mbps due to the longer allotted time and less interference. Interference is removed by ZF and, in this way, the throughput is tripled with respect to the baseline scheme, i.e., TDMA with one best link, to around 150 Mbps.

Although Rx1 and Rx2 have the same allotted time, channel gain is lower for Rx2 compared to Rx1. Thus, the throughput using TDMA with one best link is only 30 Mbps and TDMA with two best links is 44 Mbps. In TDMA with spatial reuse scheme, the data rate of Rx2 is improved to 40 Mbps compared to the baseline. In this scheme, Rx2 is used as a parallel link in the last four time slots. Using SDMA with two best links, Rx2 has a longer allotted time and less interference, and hence, the throughput increases 2.5 times to around 75 Mbps. ZF together with SDMA using two best links almost quadruples the throughput to around 118 Mbps.

Rx3, as well as Rx6, have lower channel gain as compared to other receivers. These receivers can be considered as typical “cell-edge” users having weaker channel gain and more interference when serving them in parallel to other users. Using TDMA with one best link, the throughput for Rx3 and Rx6 is around 10 Mbps and 8 Mbps, respectively. These values are improved to 25 and 22 Mbps, respectively, when using TDMA with two best links. Using TDMA with spatial reuse, throughput

is nearly the same compared to the baseline. Using SDMA with two best links, due to the significant interference from the other sources, the throughput of Rx3 and Rx6 is 18 Mbps and 15 Mbps, respectively. By nullifying the interference with ZF, throughput can be quadrupled for both users to values of 40 Mbps and 30 Mbps.

Rx4 and Rx5 have the strongest LOS signals from the intended transmitters. Thus, the throughput using TDMA with one best link is around 55 Mbps and 63 Mbps, respectively. In TDMA with two best links, the throughput is improved to 95 and 75 Mbps, respectively. Using TDMA with spatial reuse, Rx4 is receiving the signals in the first two time slots as well as in the fourth time slot. So, the individual throughput of Rx4 is around 115 Mbps. But, the throughput in Rx5 is reduced to 63 Mbps as compared to TDMA with two best link. Using SDMA with two best links, due to lower interference from other transmitters, the throughput is increased to around 125 Mbps and 100 Mbps, respectively. Finally, the ZF method nullifies the interference and the throughput is further improved to around 135 Mbps and 113 Mbps, respectively.

From these results, it becomes clear that SDMA with ZF offers the best overall individual user throughput. Moreover, it is obvious that the same scheme leads to enhanced fairness among the users. The use of this scheme is most beneficial for all the users, but particularly at the cell edge, where it improves the performance significantly compared to users at other locations. Note that, access points and users have to be selected carefully. They should be sufficiently distant, as demonstrated in [35]. Usually, different MIMO modes are available at the medium access control (MAC) layer. In a mobile scenario, the scheduler will always switch to the best performing MIMO mode. The criterion is based on comparing the individually achievable user throughput for each available MIMO mode. Switching to the best overall MIMO mode is usually done in an opportunistic and fair manner [38], [39].

The total throughput for all multiplexing schemes of the 4x6 distributed MU-MIMO system is shown in Fig. 7(b). As expected from the results for each individual receivers, TDMA with one best link has the lowest throughput of around 220 Mbps. The throughput improves to around 300 Mbps when combining the two best links. In the spatial reuse scheme, even though we utilize the spatial multiplexing, throughput is reduced to 280 Mbps due to the interference. The advantages of spatial multiplexing are attained when interference-limited SDMA with two best links is applied leading to an overall throughput of about 430 Mbps. This is similar to the well known “soft handover” advantage in cellular networks, i.e., serving one user from its best two base stations [40]. When it is combined with interference cancellation, using SDMA with ZF, overall throughput is further increased to around 600 Mbps, i.e.,  $\sim 2.5$  times improvement over the baseline TDMA with one best link scheme and  $\sim 1.5$  times over the interference-limited SDMA with two best links scheme. Note that, in our scenario when there are more users, the overall system throughput is likely to increase, because there are more opportunities to combine users for joint transmission (multi-user diversity). However, the individual user throughput will reduce due to sharing of time and space resources.

## VII. CONCLUSION

In this paper, we have described the first experimental study of LiFi channels based on LiFi channel measurements in an operating room. While both LOS and NLOS links have been studied, we observed that the availability of the LOS links are favorable for high data rate services. From the experimental data, we observed that the measured channel responses and parameters strongly depend on the position of optical frontends, link blockage, and diffuse reflections.

For efficient communication in the LiFi scenario between multiple frontends, we proposed the possibility of extending the single link LOS channel responses into a distributed MU-MIMO system. In this way, we have studied how to improve reliability through spatial diversity when the LOS is blocked and increase data rates through spatial multiplexing. For the measured MIMO channel matrix in our medical scenario, we found two main singular values which create the possibility to support at least two parallel data streams.

To fully benefit from the parallel data transmission, different multiuser scheduling schemes such as *i*) TDMA with one best link; *ii*) TDMA with two best links; *iii*) TDMA with spatial reuse; *iv*) SDMA with two best links; and *v*) SDMA with ZF were considered. A uniform mathematical framework for these schemes was proposed and performance was evaluated for each multiplexing schemes.

As a major takeaway from this study, we first need to select the best transmitters for each receiver and then combine them for joint transmission. This will provide the required spatial diversity and enhance reliability against potential blockage. Later, in each time slot, by selecting the second user for parallel communication, joint processing based on the effective MU-MIMO channel matrix brings a further improvement in the performance. In this way, also the complexity of the 4x6 MU-MIMO system reduces significantly to an effective 2x2 MIMO link in each time slot. For all scheduling schemes, we have estimated the effective SINR and the achievable throughput. We noticed the impressive impact of SDMA-ZF method on the performance of every Rx, especially those at cell edge. The total throughput is  $\sim 220$  Mbps using TDMA with one best link,  $\sim 300$  Mbps using TDMA with two best links,  $\sim 280$  Mbps using TDMA with spatial reuse,  $\sim 430$  Mbps using SDMA with two best links, and  $\sim 600$  Mbps using SDMA with ZF. Hence, the throughput is  $\sim 2.7$  times higher when using SDMA with ZF compared to the baseline TDMA with one best link scheme.

Overall, we have demonstrated the potential of using LiFi in indoor hospital scenarios and highlighted the main steps for reliable, secure and efficient optical wireless communication. By using appropriate MU-MIMO schemes, reliability can be improved and the data rate can be increased with reasonable system complexity.

## APPENDIX

### A. NLOS Channel Measurements

Under NLOS conditions, three different measurement scenarios are considered, as shown in Fig. 8. In the first NLOS scenario

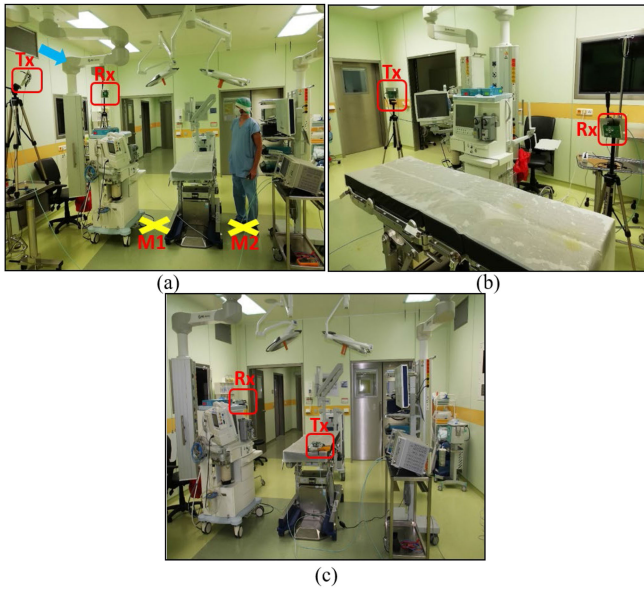


Fig. 8. NLOS LiFi-configurations; (a) the Tx and Rx point towards the table and a person stands at 2 positions M1 and M2, the movable ceiling mounted arm system marked as a blue arrow (scenario 1). (b) Tx and Rx point towards the operating table and Rx is tilted in the horizontal and vertical direction (scenario 2). (c) Tx and Rx point towards the ceiling (scenario 3).

(Fig. 8(a)), both Tx and Rx are fixed near the ceiling and point towards the operating table. The LOS link between the Tx and Rx is blocked by a movable ceiling-mounted arm system. In order to study a possible influence of a person (e.g., doctor or assistant) moving around the operating table, the measurements are also performed with a person standing at two different positions, M1 and M2. The position M1 is on the right side of the operating table with coordinates (4.7 m, 2.2 m) and close to Tx and Rx, while M2 is on the left side and far from Tx and Rx with coordinates (4.7 m, 3.3 m). In the second NLOS scenario (Fig. 8(b)), a medical instrument blocks the LOS-link. In this case, the Tx and Rx are pointed towards the operating table. Here, we investigated the tilt of Rx in the horizontal and vertical direction at different positions P1-P5. Finally, in the third NLOS scenario (Fig. 8(c)), ceiling reflections are evaluated. To that aim, the Rx is fixed near the operation table pointing towards the ceiling. The Tx is positioned on the operating table at two different positions, N1 and N2. Here, N1 corresponds roughly to the head position of the patient, and N2 to the leg position of the patient during an operation. Since Rx and Tx are pointed towards the ceiling, diffuse reflections are observed in this configuration. The exact positions and tilt angles of Tx and Rx corresponding to each scenario are given in Table II.

### B. NLOS Channel Measurement Results

The channel amplitude response of NLOS configurations in the three scenarios, described in Section II, are shown in Fig. 9. In general, the signal is much weaker, due to both, the blockage of the LOS and the diffuse nature of signal reflections. Among multiple NLOS paths, there may be destructive interference at certain frequency if two signals arrive with similar power and opposite phase.

TABLE II  
POSITIONS AND TILT ANGLES OF OPTICAL FRONTENDS IN  
NLOS CONFIGURATIONS

NLOS Scenarios	Positions in m ( $x, y, z$ )	Tilt angle (+ve and -ve of horizontal tilt angle indicates clockwise and anti-clockwise directions)
Scenario 1: Tx	(3.5, 4.31, 1.93)	30° vertical down and -30° horizontal with respect to -Y axis
Scenario 1: Rx	(5.67, 4.55, 2.1)	30° vertical down and +30° horizontal with respect to -Y axis
Scenario 2: Tx	(3.05, 3.67, 1.33)	30° vertical down and -60° horizontal with respect to -Y axis
Scenario 2: Rx at P1	(5.98, 3.67, 1.4)	0° tilt with respect to -Y axis
Scenario 2: Rx at P2	(6.02, 3.69, 1.4)	-30° horizontal with respect to -Y axis
Scenario 2: Rx at P3	(5.94, 3.69, 1.4)	+30° horizontal with respect to -Y axis
Scenario 2: Rx at P4	(5.98, 3.69, 1.36)	30° vertical down direction with respect to -Y axis
Scenario 2: Rx at P5	(5.98, 3.69, 1.44)	30° vertical up direction with respect to -Y axis
Scenario 3: Tx at N1	(4.4, 2.7, 1)	0° tilt with respect to +Z axis
Scenario 3: Tx at N2	(6, 2.7, 1)	0° tilt with respect to +Z axis
Scenario 3: Rx	(4.67, 3.8, 1.47)	0° tilt with respect to +Z axis

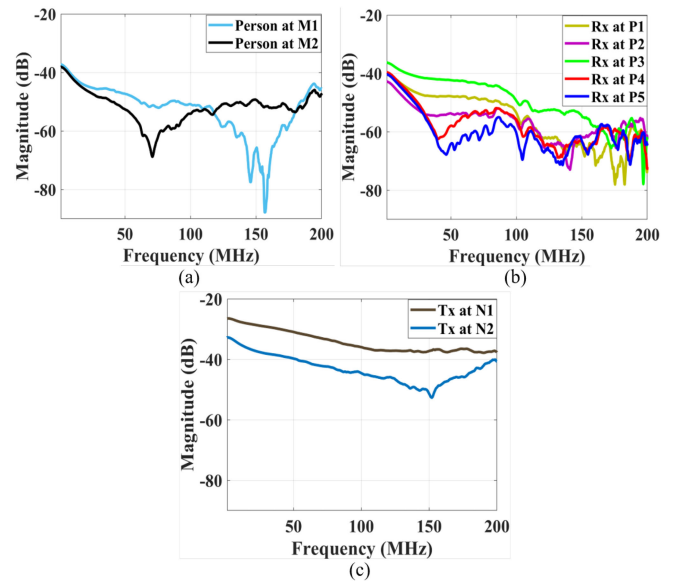


Fig. 9. Amplitude responses of LiFi channels in NLOS configurations: (a) scenario 1, (b) scenario 2, and (c) scenario 3.

In Fig. 9(a), the results for NLOS links in scenario 1 are shown, where a person stands at two different positions, M1 and M2, respectively. As mentioned above, fading occurs in NLOS links due to the different path delays of reflected signals in the environment. In this case, one can observe that the fading, varies significantly from higher frequencies around 150 MHz to lower frequencies at 70 MHz when the person moves from far side position M1 to the near side position M2 concerning the Tx or Rx positions. The amplitude responses of the channels corresponding to NLOS scenario 2 are shown in Fig. 9(b). In this case, a medical instrument blocks the LOS link, the Rx is

TABLE III  
CHANNEL PARAMETERS FOR NLOS SCENARIOS

Scenario	Path loss (electrical dB)	RMS Delay spread (ns)
Scenario 1: Person standing at M1	37.3	9.1
Scenario 1: Person standing at M2	38.1	10.0
Scenario 2: Rx at P1	39.8	7.4
Scenario 2: Rx at P2	42.8	9.9
Scenario 2: Rx at P3	36.3	5.3
Scenario 2: Rx at P4	39.6	9.6
Scenario 2: Rx at P5	40.3	10.0
Scenario 3: Tx at N1	26.5	2.9
Scenario 3: Tx at N2	32.7	5.3

tilted in the horizontal as well as in the vertical direction. In this case, the power of the received signal is higher only if the Rx FOV point towards the area illuminated by the Tx. Due to higher-order reflections, the channel frequency response above 100 MHz has more fading in general. Here, the receivers at P1 and P3 have better reception at frequencies below 100 MHz, where other cases have very weak signal and a drop of more than 10 dB at frequencies below 100 MHz.

The amplitude responses of the channels in NLOS scenario 3 are shown in Fig. 9(c). In this case, the signal amplitude is significantly higher due to reflections from the ceiling. Due to high reflectivity of the ceiling, here we observed no steep drops or fading effects and a high gain in the channel response. The signal would be stronger if Tx and Rx positions are closer to each other and weaker if separated. For the Tx at N1, we observed more than 12 dB increased channel gain when compared to the previous NLOS scenarios. Such a NLOS link has a good quality, which is comparable to LOS links. However, in a real environment, such an unperturbed NLOS link will be difficult to achieve.

Table III shows the channel parameters for the considered NLOS scenarios. Path loss is mainly due to different optical absorption coefficients of the materials and, partially to the distance between the optical frontends. Similar to LOS scenarios, path loss and RMS delay, are lower for strong NLOS links and higher for scenarios with weak NLOS links.

ACKNOWLEDGMENT

The authors would like to acknowledge the Department of Neurosurgery, 2nd Faculty of Medicine, Charles University in Prague and Motol University Hospital, Prague, Czech Republic for all the provided help during experiments.

REFERENCES

[1] H. Haas, L. Yin, Y. Wang, and C. Chen, "What is lifi?," *J. Lightw. Technol.*, vol. 34, no. 6, pp. 1533–1544, Mar. 2016.  
 [2] H. Haas *et al.*, "Introduction to indoor networking concepts and challenges in LiFi," *J. Opt. Commun. Netw.*, vol. 12, no. 2, pp. A190–A203, 2020.  
 [3] I. Ahmed, H. Karvonen, T. Kumpulinen, and M. Katz, "Wireless communications for the hospital of the future: Requirements, challenges and solutions" *Int. J. Wireless Inf. Netw.*, vol. 27, pp. 4–17, 2020.

[4] A. Holzinger, C. Rocker, and M. Zieffe, "From smart health to smart hospitals," in *Smart Health LNCS*, Heidelberg, Germany: Springer, 2015, pp. 1–20.  
 [5] S. B. Baker, W. Xiang, and I. Atkinson, "Internet of things for smart healthcare: Technologies, challenges, and opportunities," *IEEE Access*, vol. 5, pp. 26521–26544, 2017.  
 [6] O. Gutiérrez, M. Navarro, F. Adana, A. Escobar, M. Moncada, and C. Muñoz, "Study of electromagnetic compatibility in hospital environments," *J. Electromagn. Anal. Appl.*, vol. 6, no. 7, pp. 141–155, 2014.  
 [7] L. Grobe *et al.*, "High-speed visible light communication systems," *IEEE Commun. Mag.*, vol. 51, no. 12, pp. 60–66, Dec. 2013.  
 [8] M. Z. Chowdhury, M. Shahjalal, M. K. Hasan, and Y. M. Jang, "The role of optical wireless communication technologies in 5G/6G and IoT solutions: Prospects, directions, and challenges," *Appl. Sci.*, vol. 9, no. 20, Jan. 2019.  
 [9] A. Khalid, G. Cossu, and E. Ciaramella, "Diffuse IR-optical wireless system demonstration for mobile patient monitoring in hospitals," in *Proc. 15th Int. Conf. Transparent Opt. Netw. (ICTON)*, Jun. 2013, pp. 1–4.  
 [10] R. Murai *et al.*, "A novel visible light communication system for enhanced control of autonomous delivery robots in a hospital," in *IEEE Int. Symp. Syst. Integration*, 2012, pp. 510–516, doi: 10.1109/SII.2012.6427311.  
 [11] L. Chevalier, S. Sahuguede, and A. Julien-Vergonjanne, "Optical wireless links as an alternative to radio-frequency for medical body area networks" *IEEE J. Sel. Areas Commun.*, vol. 33, no. 9, pp. 2002–2010, Sep. 2015, doi: 10.1109/JSAC.2015.2432527.  
 [12] O. Haddad, M. A. Khalighi, S. Zvanovec, and M. Adel, "Channel characterization and modeling for optical wireless body-area networks," *IEEE Open J. Commun. Soc.*, vol. 1, pp. 760–776, Jun. 2020.  
 [13] P. Chvojka, S. Zvanovec, P. A. Haigh, and Z. Ghassemlooy, "Channel characteristics of visible light communications within dynamic indoor environment," *J. Lightw. Technol.*, vol. 33, no. 9, pp. 1719–1725, May 2015.  
 [14] I. Ahmed, T. Kumpulinen, and M. Katz, "A hybrid optical-radio wireless network concept for the hospital of the future," in *Proc. 13th EAI Int. Conf. Body Area Netw.*, Oulu, 2018, pp. 157–170.  
 [15] J. Song *et al.*, "Indoor hospital communication systems: An integrated solution based on power line and visible light communication," in *Proc. IEEE Faible Tension Faible Consommation (FTFC)*, May 2014, pp. 1–6.  
 [16] Y. Y. Tan and W. Y. Chung, "Mobile health-monitoring system through visible light communication," *Bio-Med. Mater. Eng.*, vol. 24, no. 6, pp. 3529–3538, Sep. 2014.  
 [17] S. S. Torkestani, S. Sahuguede, A. Julien-Vergonjanne, and J. P. Cances, "Indoor optical wireless system dedicated to healthcare application in a hospital," *IET Commun.*, vol. 6, no. 5, pp. 541–547, Mar. 2012.  
 [18] V. Jungnickel *et al.*, "Optical wireless communication for backhaul and access," in *Proc. Eur. Conf. Opt. Commun. (ECOC)*, Valencia, vol. 1, 2015, pp. 1–3.  
 [19] P. Wilke Berenguer *et al.*, "Optical wireless MIMO experiments in an industrial environment," *IEEE J. Sel. Areas Commun.*, vol. 36, no. 1, pp. 185–193, Jan. 2018.  
 [20] P. W. Berenguer *et al.*, "Real-time optical wireless mobile communication with high physical layer reliability," *J. Lightw. Technol.*, vol. 37, no. 6, pp. 1638–1646, Mar. 2019.  
 [21] S. M. Mana *et al.*, "LiFi experiments in a hospital," in *Opt. Fiber Commun. Conf. (OFC)*, Mar. 2020, Paper M31.2.  
 [22] S. M. Mana, P. Hellwig, J. Hilt, P. W. Berenguer and V. Jungnickel, "Experiments in Non-Line-of-Sight li-fi channels," in *Global LIFI Congress (GLC)*, Paris, France, 2019, pp. 1–6.  
 [23] J. M. Kahn and J. R. Barry, "Wireless infrared communications," *Proc. IEEE*, vol. 85, no. 2, pp. 265–298, 1997.  
 [24] V. Jungnickel, V. Pohl, S. Nonnig, and C. von Helmolt, "A physical model of the wireless infrared communication channel," *IEEE J. Sel. Areas Commun.*, vol. 20, no. 3, pp. 631–640, Apr. 2002.  
 [25] M. K. Karakayali, G. J. Foschini, and R. A. Valenzuela, "Network coordination for spectrally efficient communications in cellular systems," *IEEE Wireless Commun.*, vol. 13, no. 4, pp. 56–61, Aug. 2006.  
 [26] R. Irmer *et al.*, "Coordinated multipoint: Concepts, performance, and field trial results," *IEEE Commun. Mag.*, vol. 49, no. 2, pp. 102–111, Feb. 2011.  
 [27] K. L. Bober *et al.*, "Distributed multiuser MIMO for lifi in industrial wireless applications," *J. Lightw. Technol.*, vol. 39, no. 11, pp. 3420–3433, Jun. 2021.  
 [28] S. Al-Ahmadi, O. Maraqa, M. Uysal, and S. M. Sait, "Multi-user visible light communications: State-of-the-art and future directions," *IEEE Access*, vol. 6, pp. 70555–70571, Nov. 2018.  
 [29] C. Chen, Y. Yang, X. Deng, P. Du, and H. Yang, "Space division multiple access with distributed user grouping for multi-user MIMO-VLC systems," *IEEE Open J. Commun. Soc.*, vol. 1, pp. 943–956, Jul. 2020.

- [30] J. Beysens, J. P. M. G. Linnartz, D. Van Wageningen, and S. Pollin, "TDMA scheduling in spatially extended lifi networks," *IEEE Open J. Commun. Soc.*, vol. 1, pp. 1524–1538, Sep. 2020.
- [31] G. Lebrun, J. Gao, and M. Faulkner, "MIMO transmission over a time-varying channel using SVD," *Wireless Communications, IEEE Trans.*, vol. 4, no. 2, pp. 757–764, Mar. 2005.
- [32] V. Jungnickel *et al.*, "Capacity measurements in a cooperative MIMO network," *IEEE Trans. Veh. Technol.*, vol. 58, no. 5, pp. 2392–2405, 2009.
- [33] Q. H. Spencer, C. B. Peel, A. L. Swindlehurst, and M. Haardt, "An introduction to the multi-user MIMO downlink," *IEEE Commun. Mag.*, vol. 42, no. 10, pp. 60–67, Oct. 2004.
- [34] ITU-T. Unified high-speed wireline-based home networking transceivers – system architecture and physical layer specification. Series G: Transmission Systems and Media, Digital Systems and Networks, G.9960, 2015. [Online]. Available: <https://www.itu.int/rec/T-REC-G.9960-201507-S/en>
- [35] S. M. Mana, S. M. Kouhini, P. Hellwig, J. Hilt, P. W. Berenguer, and V. Jungnickel, "Distributed MIMO experiments for lifi in a conference room," in *Proc. 12th Int. Symp. Commun. Syst., Netw. Digit. Signal Process. (CSNDSP)*, 2020.
- [36] C. E. Shannon, "Communication in the presence of noise," *Proc. IRE*, vol. 37, no. 1, pp. 10–21, Jan. 1949.
- [37] Q. Spencer, A. Swindlehurst, and M. Haardt, "Zero-Forcing methods for downlink spatial multiplexing in multiuser MIMO channels" in *IEEE Trans. Signal Process.*, vol. 52, no. 2, pp. 461–471, Feb. 2004.
- [38] L. Thiele, V. Jungnickel, M. Schellmann, and W. Zirwas, "Capacity scaling of multi-user MIMO with limited feedback in a multi-cell environment," in *Proc. Conf. Rec. 41st Asilomar Conf. Signals, Syst. Comput.*, Pacific Grove, CA, USA, 2007, pp. 93–100.
- [39] M. Schellmann, L. Thiele, T. Haustein and V. Jungnickel, "Spatial transmission mode switching in multiuser MIMO-OFDM systems with user fairness," *IEEE Trans. Veh. Technol.*, vol. 59, no. 1, pp. 235–247, Jan. 2010.
- [40] A. J. Viterbi, A. M. Viterbi, K. S. Gilhousen, and E. Zehavi, "Soft handoff extends CDMA cell coverage and increases reverse link capacity," *IEEE J. Sel. Areas Commun.*, vol. 12, no. 8, pp. 1281–1288, Oct. 1994.

**Sreelal Maravanchery Mana** received the M.Tech. degree in optical engineering from the Indian Institute of Space Science and Technology, Thiruvananthapuram, India, in 2017. He is currently working toward the Ph.D. degree in optical wireless communications. Since August 2018, he has been a Marie Curie Research Fellow with the Department of Photonic Networks and Systems, Fraunhofer Institute for Telecommunications, Heinrich Hertz Institute, Berlin, Germany. His current research interests include the channel modeling simulation and experiments for optical wireless communication systems, MU MIMO for LiFi networks, and DCO-OFDM systems.

**Volker Jungnickel** (Member, IEEE) received the Doctoral degree in experimental physics from Humboldt University, Berlin, Germany, in 1995, and the Habilitation degree in communications engineering from the Technical University of Berlin, Berlin, Germany, 2015. In 1997, he joined Fraunhofer HHI, Berlin, Germany, working on optical wireless communication, adaptive multiple antenna techniques in mobile networks, and fixed optical access infrastructures. He is with the Technical University of Berlin as Privatdozent teaching courses on advanced wireless communications and supervising master's and Ph.D. thesis. He is the Chair of IEEE P802.15.13 Task Group on multi-Gbit/s optical wireless communications and the Technical Editor of the IEEE P802.11bb Task Group on light communications.

**Kai Lennert Bober** (Student Member, IEEE) received the M.Eng. degree in computer engineering from the Technical University of Berlin, Berlin, Germany, in 2018. He is with the Department of Photonic Networks and Systems, Fraunhofer Institute for Telecommunications, Heinrich Hertz Institute, Berlin, Germany, since 2016. He is currently working on optical wireless communications, including the development of prototypes and research towards realization aspects of distributed MIMO LiFi systems. He is also the Technical Editor of the IEEE P802.15.13 Task Group on Multi-Gbit/s Optical Wireless Communications.

**Peter Hellwig** received the Diploma degree in electrical engineering from the Berlin University of Applied Sciences, Berlin, Germany, in 2009. In 2016, he joined the Fraunhofer Institute for Telecommunications, Heinrich Hertz Institute, where he works as an Electrical Engineer with the Department of Photonic Networks and Systems. His current interests include the area of design and realization of optical wireless communication systems.

**Jonas Hilt** received the Diploma degree in electrical engineering from the Berlin University of Applied Sciences, Berlin, Germany, in 2009. In 2009, he joined the Fraunhofer Institute for Telecommunications, Heinrich Hertz Institute, Berlin, Germany, where he is an Electrical Engineer with the Department of Photonic Networks and Systems. His current interests include the area of design and realization of embedded systems and optical wireless communication systems.

**Dominic Schulz** received the M.Eng. degree in communications engineering from the Berlin University of Applied Sciences, Berlin, Germany, in 2012, and the Ph.D. degree from the Technical University of Berlin, Berlin, Germany, in 2019. In 2012, he joined the Department of Photonic Networks and Systems, Fraunhofer Institute for Telecommunications, Heinrich Hertz Institute, Berlin, Germany. He is currently working in the field of optical wireless communications. His current research interests include the development of high data rate systems for wireless access and research towards short-range outdoor backhaul links for small radio cells and wireless-to-the-home.

**Anagnostis Paraskevopoulos** received the Electrical Engineering degree from Technical University in Athens, Athens, Greece and the Ph.D. degree from Université Paris-Orsay, Paris, France, with a study on RF modulation of semiconductor lasers performed at the CNET (Research Centre-France Telecom), Paris. He joined HHI in 1988 and was since involved in various research projects, including the ESPRIT263 project on HBTs, a national project on VCSEL devices at 980 nm in the early 90's and custom designed laser diodes for non-telecom applications. For more than 22 years, he has successfully coordinated R&D projects, concerning both research subjects and industrial applications. He has authored and coauthored more than 50 scientific papers. He is currently focusing on applications for optical wireless communication – LiFi.

**Ronald Freund** (Member, IEEE) received the Dipl.-Ing. and Dr.-Ing. degree in electrical engineering from the Technical University of Ilmenau, Ilmenau, Germany, in 1993 and 2002, respectively, and the MBA degree from RWTH Aachen University, Aachen, Germany. In 1997, he co-founded VPI Systems Inc., where he was the Chief Technology Officer and Consultant, responsible for the development of design software for the physical layer of photonic networks. Since 1995, he has been with Heinrich Hertz Institute, Berlin, Germany, where he is currently leading the Department of Photonic Networks and Systems. In 2017, he has been appointed as a Professor of photonic communication systems with the Technical University of Berlin, Berlin, Germany. He has authored or coauthored more than 150 scientific publications.

**Klara Hirmanova** biography not available at the time of publication.

**Radek Janca** received the M.Sc. and Ph.D. degrees from the Faculty of Electrical Engineering, Czech Technical University in Prague, Prague, Czechia, in 2010 and 2014, respectively. He is currently a Neuroscientist in epilepsy. He mainly focuses on digital signal processing of intracranial EEG, effective connectivity, neuroimaging (CT, MR, PET), data-mining, and artificial intelligence to develop novel diagnostic and treatment approaches for surgical treatment of epilepsy. He is a Researcher and Teacher with the Faculty of Electrical Engineering, Czech Technical University in Prague, Prague, Czechia and Motol University Hospital, Charles University in Prague, Prague, Czechia.

**Petr Chvojka** received the M.Sc. and Ph.D. degrees from the Faculty of Electrical Engineering, Czech Technical University (CTU) in Prague, Prague, Czechia, in 2013 and 2018, respectively. He was a Research Fellow with the Department of Electromagnetic Field, CTU in Prague focusing on optical systems design and modelling, including inorganic and organic devices and digital signal processing techniques for visible light communications as a Member of the Wireless and Fiber Optics Group. Until 2020, he was with CTU in Prague, when he joined the ComAp company developing solutions for power generation and engine control.

**Stanislav Zvanovec** (Senior Member, IEEE) received the M.Sc. and Ph.D. degrees from the Faculty of Electrical Engineering, Czech Technical University in Prague, Prague, Czechia, in 2002 and 2006, respectively. He is currently a Full Professor and the Deputy Head of the Department of Electromagnetic Field. He is the author of two books and coauthor of the book *Visible Light Communications: Theory and Applications*, several book chapters and more than 300 journal articles and conference papers. His current research interests include free space optical systems, visible light communications, fiber optical systems systems and sensors, and RF (millimeter wave) over optics.